Journal of The Electrochemical Society, 2021 **168** 040515

Electrochemically Stable In Situ Dilatometry of NMC, NCA and Graphite Electrodes for Lithium-Ion Cells Compared to XRD Measurements

Franz B. Spingler,[1,*,z] Simon Kücher,[1] Robert Phillips,[1] Erfan Moyassari,[1] and Andreas Jossen[1,2]

[1]*Institute of Electrical Energy Storage Technology, Technical University of Munich (TUM), 80333 Munich, Germany*
[2]*Munich School of Engineering (MSE), Technical University of Munich (TUM), 85748 Garching, Germany*

Virtually all types of electrodes used in lithium-ion batteries expand and contract during cycling, which poses an engineering and design challenge. Information provided by X-ray diffraction (XRD) about alterations in the crystal structure of active materials may be insufficient to inform these engineering tasks. This is because it is unclear how these evolutions of the crystal structure translate into the measurable thickness changes at the electrode or cell level. In this study we investigate the thickness changes of electrodes during cycling using a dilatometry setup and compare them to XRD-measured crystal structure changes from scientific literature. Both the reliability of the dilation measurement and the electrochemical performance of the dilatometry setup are thoroughly validated and significantly exceed those of related studies that have been published in recent years. Various laboratory-made graphites as well as $LiNi_{1/3}Co_{1/3}Mn_{1/3}O_2$ (NMC111), $LiNi_{0.6}Co_{0.2}Mn_{0.2}O_2$ (NMC622), $LiNi_{0.8}Co_{0.1}Mn_{0.1}O_2$ (NMC811) and $LiNi_{0.8}Co_{0.15}Al_{0.05}O_2$ (NCA) electrodes and the positive electrode from a Kokam SLPB356495 pouch cell are investigated. The results show that electrode expansion does not necessarily correlate with the unit cell volume changes of its active materials in any meaningful way and thus only by measuring the expansion of the full electrode can we fully understand and predict its behavior during cycling.
 [DOI: 10.1149/1945-7111/abf262]

Manuscript submitted February 11, 2021; revised manuscript received March 12, 2021. Published April 7, 2021.

Supplementary material for this article is available online

When a lithium-ion battery is charged or discharged, lithium ions intercalate and deintercalate from their host lattices in the positive and negative electrodes. Depending on the host material, the intercalation process is accompanied by an expansion or contraction in the volume of the host lattice. The magnitude of the host lattice volume change between 0% and 100% SOC can be measured via X-ray diffraction (XRD) and for full lithiation, range from 0%−2% in the case of transition-metal-oxides (TMOs) over ca. 12% for graphite to 280% in the case of silicon.[1,2] Although measuring the host lattice volume change is helpful in the understanding of interparticle stresses, which may lead to microscopic cracks and progressive film formation,[3,4] the quantity of interest in this study is the bulk expansion of practical electrodes: Knowledge of how electrodes expand and contract upon lithiation can guide battery housing/module design,[5] improve battery diagnostics based on cell expansion or pressure,[6,7] help in the assessment of the mechanical stress batteries experience in operation and provide feedback for electrode design. The latter point is especially significant for graphite/silicon composites, where the large volumetric expansion of the silicon lattice must be contained by the other electrode components to minimize intraparticle stress and mechanical decomposition of the bulk electrode.[8,9]

Practical electrodes are porous, have complex microstructures and contain non-active materials such as binder, all of which helps accommodate primary particle expansion. The combination of these factors dictates that the change in unit cell volume experienced by the active material's crystal structure does not unequivocally determine the electrode volume or its thickness change.

At the other end of the length scale, the expansion of multi-layer pouch cells can be measured with relative ease using optical[10–12] or tactile[13–16] methods, but the resulting measurement quantity is the superposition of the thickness changes of both the negative and positive electrodes and potentially the compression of the separator. Purpose-built electrochemical dilatometers that either employ a non-expanding counter electrode[17,18] or exclusively measure the thickness change of a single working electrode[19–21] offer more precise data on the expansion of individual electrodes.

With the help of electrochemical dilatometers, expansions as a result of complete lithiation have been measured at between 4% and 6.5% for graphite,[19,20] between 0% and 0.8% for $LiNi_{1/3}Mn_{1/3}Co_{1/3}O_2$ (NMC111)[17,18] and 1.8% for $LiCoO_2$ (LCO).[20] However, possibly due to cycling stability issues, these studies only report the first few cycles. There is also some uncertainty regarding the amount of irreversible expansion taking place in the first few cycles and the quantity of reversible expansion during long-term cycling. In a recent publication[22] using the same ECD-3-nano dilatometry cell (El-Cell GmbH) as in this work, the authors encountered severe capacity loss, which they attributed to electrode exfoliation and the separator design of the electrochemical cell. We believe that the principal reason behind the poor capacity retention in their experiments was the permeability of the cell to atmospheric gases and humidity. In this work, the ECD-3-nano cell was operated in an argon atmosphere and displayed excellent reproducibility as well as a cycling stability on par with coin cells. The dilatometry setup was used to investigate the reversible and irreversible thickness changes of a variety of electrodes. These were composed of either graphite or transition-metal-oxides containing varying proportions of nickel, manganese, aluminum and cobalt and were either prepared from powder or harvested from a commercial cell.

This paper is structured as follows: In the experimental section, electrode and coin cell preparation and the dilatometry setup as well as the cycling procedures are discussed. This is followed by a thorough validation of the dilatometry cell in regard to its electrochemical performance and the reliability of the dilation measurement. In the results section, the thickness changes measured in the electrodes of the various materials are discussed and compared to similar measurements and host lattice volume change data from XRD measurements reported in the literature.

Experimental

Electrode preparation from powder.—Electrode slurries were prepared from powders obtained from SGL, BASF and MTI Corp

*Electrochemical Society Student Member.
[z]E-mail: franz.spingler@tum.de

Table I. Coating thicknesses and porosities of the electrodes used in this study.

Type	Coating thickness/μm	Porosity/%	Active material loading/mg*cm^{-2}
Graphite (SGL)	60	40	7.28
Graphite (CSCC)	31	65	2.21
NMC 111 (BASF)	64	35	13.51
NMC 622 (BASF)	33	35	8.13
NMC 811 (MTI)	40	35	10.27
NCA (BASF)	40	35	10.00
Kokam cathode	66.5	unknown	unknown

which were dispersed in N-Methyl-2-pyrrolidinone (NMP) from Sigma Aldrich. Solef 5130 PVDF by Solvay and Kynar HSV by Arkema were used as binders and Super C65 Carbon black by Timcal as the conductive agent. All transition-metal-oxide-based slurries were prepared in a Thinky ARV-310 planetary vacuum mixer, coated on 16 μm thick aluminum foil using a table top K Control Coater by RK Print Coat Instruments, dried at 60 °C for 6 h and then compacted to a porosity of 35% using a Saueressig GK 300 l calender. Graphite slurries were prepared in a Hauschild Speedmixer DAC 3000 planetary mixer, coated and dried on 11 μm thick copper foil using a roll-to-roll Coatema BC50 coating machine with an inline infrared dryer and compacted to a porosity of 35% using a Coatema EA50 calender. The slurry recipes can be found in the Appendix in Table A·I. The slurry mixing procedures are provided in detail in the supplementary information (available online at stacks.iop.org/JES/168/040515/mmedia). The final coating thicknesses and porosities of the electrodes are summarized in Table I.

Harvested electrodes from a commercial cell.—A fresh 2.1 Ah Kokam SLPB 356495 cell was discharged at 0.1 C to 3.0 V and disassembled in an argon filled glovebox (<0.1 ppm H_2O/O_2). Before cutting out 10 mm disks (for the dilatometry cell) and 14 mm disks (for coin cells) with a handheld precision punch (Nogamigiken Co.), the coating of the anode sheets was pulled off on one side using off-the-shelf isolating tape. Attempts were also made to remove the coating by scraping it off using a scalpel and by rubbing it off using an electrical oscillating toothbrush in combination with various solvents (diethyl carbonate, acetone and NMP) but the pull-off method resulted in the best electrochemical performance and reproducibility in both the coin cells and the dilatometry cell. After testing both non-washed samples and samples washed in diethyl carbonate for 3 min, it was decided to use non-washed samples for the same reasons as above. In the case of the cathodes, no coating removal was necessary because the two outermost cathode sheets of these cells are single-side coated. The disks were left to dry inside the glovebox for at least 24 h before being used in coin cells or the dilatometry cell.

Coin cell preparation.—CR2032-type coin cells were prepared inside an argon-filled glovebox using two layers of 16.0 mm diameter VWR 691 glass fiber (260 μm each) as the separator, a 15.6 mm lithium chip as the counter electrode and two spacers of 1.0 mm and 0.5 mm thickness. The working electrode diameter was 14.0 mm. 80 μl of LP57 (3:7 wt. EC:EMC 1 M LiPF6) was used as electrolyte solution.

Dilatometry cell.—The dilation experiments were conducted using an ECD-3-nano dilatometry cell from El-Cell GmbH which uses a capacitive displacement sensor. The sensor resolution is specified by the manufacturer at 5 nm and drift at 20 nm h^{-1}. Figure 1 shows a schematic of the setup. The electrochemical cell holds working electrodes of 10 mm diameter. A 12 mm diameter lithium chip (250 μm) serves as counter electrode. Working and counter electrode are separated by a porous borosilicate glass separator. A blind bore filled with lithium at the end of a metal tip

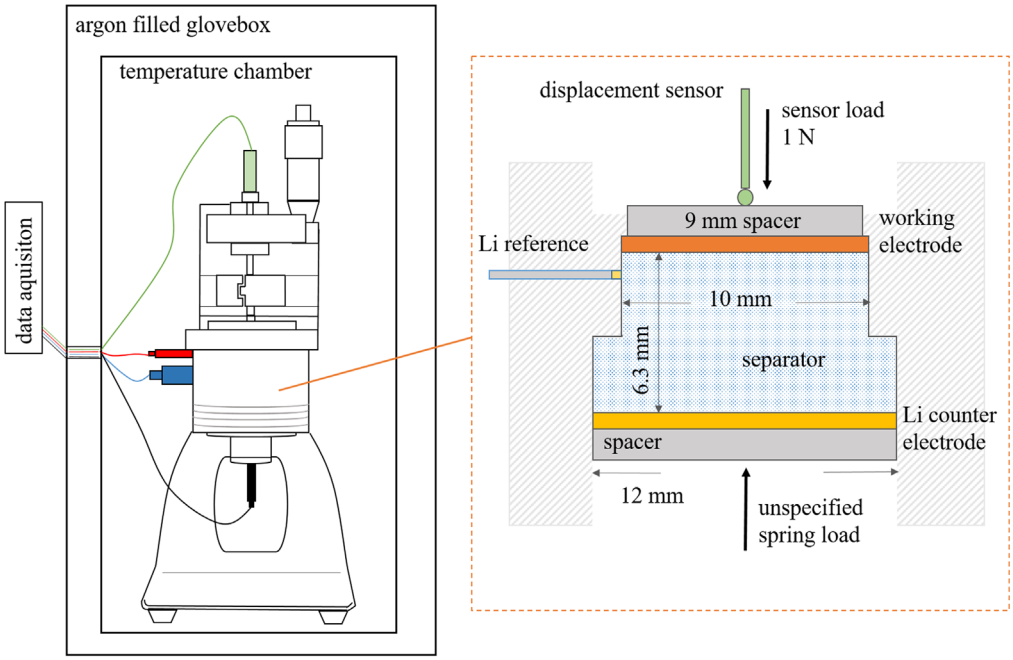

Figure 1. Schematic of dilatometry cell setup in temperature-controlled argon atmosphere and of the electrochemical cell with a t-shaped frit, which shields the displacement measurement of the working electrode from any dilation that may occur in the counter electrode.

serves as reference electrode and touches the separator from the side. The separator has a thickness of 6.3 mm which causes significant overpotentials during charging and discharging of the cell. A series of experiments in temperature-controlled ambient air, where the reversible capacity deteriorated quickly, suggested that the dilatometry cell is insufficiently airtight. It was subsequently operated in a custom-built temperature chamber inside an argon filled glovebox, resulting in low rates of capacity loss comparable with those seen in coin cells.

Cycling procedures.—After assembly, both coin cells and the dilatometry cell were rested for 6 h and then cycled using a constant current charge/constant current discharge protocol (CC/CC). If not otherwise specified, graphite electrodes were cycled at a current density of 75 μA cm^{-2} and transition-metal-oxide electrodes were cycled at a current density of 180 μA cm^{-2}. The areal current densities were kept constant within the graphite and transition-metal-oxide groups in order to keep the dominant overpotential across the separator constant. This results in varying C-rates between C/8 and C/33, which are indicated in every figure along with the areal current density. The low current density for the graphite electrodes was chosen to get as close as possible to full lithiation despite the relatively large overpotentials of the dilatometry cell. The overpotentials are less of a limitation when cycling transition-metal-oxide electrodes because they can be compensated for by placing the cut-off potentials lower or higher than the desired equilibrium potentials at the end of charge/discharge. The graphite electrodes were cycled between 10 mV and 1.5 V. The transition-metal-oxide electrodes were cycled in four voltage windows between 3 V and four different upper cut-offs: 4.1 V, 4.3 V, 4.5 V and 4.7 V. Three cycles took place in each voltage window. After numerous validation experiments with all of the tested electrode materials, the final experiments shown in the results section were generally not repeated unless indicated otherwise.

Validation of the Dilatometry Setup

Chamber/cell temperature.—Preliminary experiments with the dilatometry cell had shown large overpotentials on charge and discharge, which were attributed to the cell design, more specifically the relatively thick borosilicate glass separator. As a countermeasure, it was decided to use a higher chamber temperature of 35 °C instead of the standard 25 °C, which was expected to have a positive effect on ion transport through the separator. To better understand the impact of the temperature change, the temperature was increased from 25 °C to 35 °C five cycles into a measurement on a graphite electrode. After 10 h of resting to let the temperature in the cell equalize, cycling was resumed. Figure 2a shows the electrode voltage vs Li/Li+ and the thickness change measured by the sensor. It can be seen that at 35 °C the voltage during lithiation was slightly higher, indicating less polarization, and that a higher cell capacity was reached. Moreover, it was found that the displacement signal fluctuated less. Figure 2b illustrates the likely cause: The Peltier-element-powered temperature chamber was less able to maintain a steady temperature at 25 °C than at 35 °C, possibly due to elevated temperatures inside the glove box itself on summer days. The chamber temperature for all dilatometry experiments was thus set at 35 °C. The temperature dependence of the displacement signal will be discussed in more detail at the end of this chapter.

Electrochemical performance of the dilatometry cell (vs coin cells).—In order to assess the electrochemical performance of the dilatometry cell, the voltage characteristics, specific capacity and charge/discharge efficiency of a graphite electrode were compared to those of 2032 coin cells, which serve as a reference. Figure 3 shows the voltage profile vs specific capacity of the 15th cycle. In the case of the coin cell, the full cell voltage of a graphite/lithium cell is shown, while in the case of the dilatometer, the graphite electrode potential vs the lithium reference is shown. The areal current densities in both cells were set at 75 μA cm^{-2}. The coin cell reached a specific capacity on delithiation of 366 mAh g^{-1} compared to 357 mAh g^{-1} in the dilatometry cell, a difference of 2.5%. This may be explained by larger overpotentials in the dilatometry cell: In the LiC_{12}/LiC_6 plateau between ~200 mAh g^{-1} and ~350 mAh g^{-1}, there is a 4 mV difference between the potentials of the dilatometry cell and the coin cell. One reason may be the distance of 2 −3 mm (in perpendicular direction to the electrode surface) between the reference electrode tip and the working electrode.

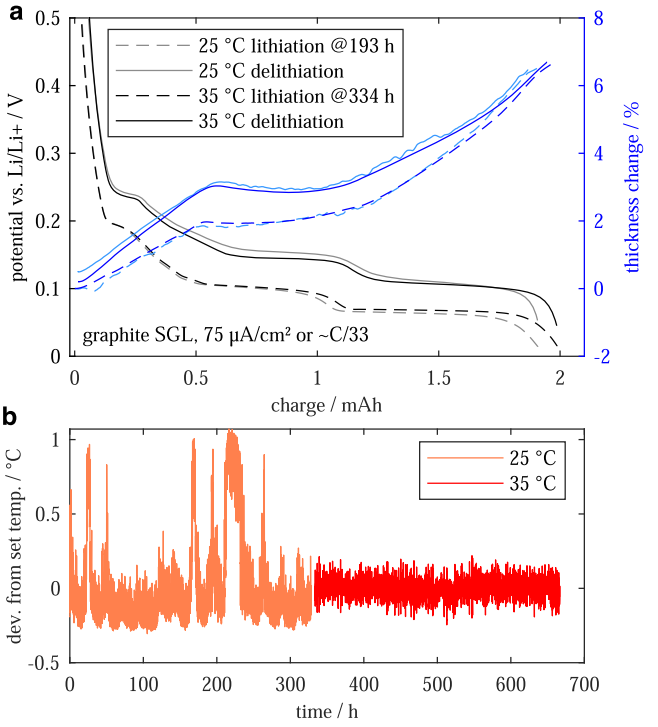

Figure 2. (a) Potential and height change vs the amount of charge in a graphite electrode when cycled at 25 °C and 35 °C. (b) temperature deviation vs time in the instrument chamber for the two set temperatures. The temperature deviations at 25 °C correlate with deviations in the displacement sensor signal. At 35 °C, In addition to a smoother signal, the obtained capacity of the graphite electrode was ca. 4% higher.

Figure 4 shows charge/discharge capacities and coulombic efficiencies of both cell types over a period of 1500 h or ca. 50 cycles. The dilatometry cell had a lower coulombic efficiency in the

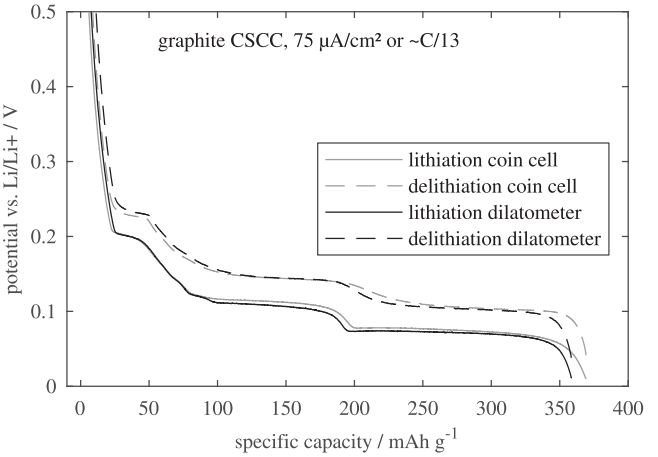

Figure 3. Comparison of potential vs specific capacity of a graphite electrode cycled in a coin cell and in the dilatometry cell using the same area specific current. The polarization in the dilatometry cell is slightly larger, resulting in ca. 3 % lower capacity utilization.

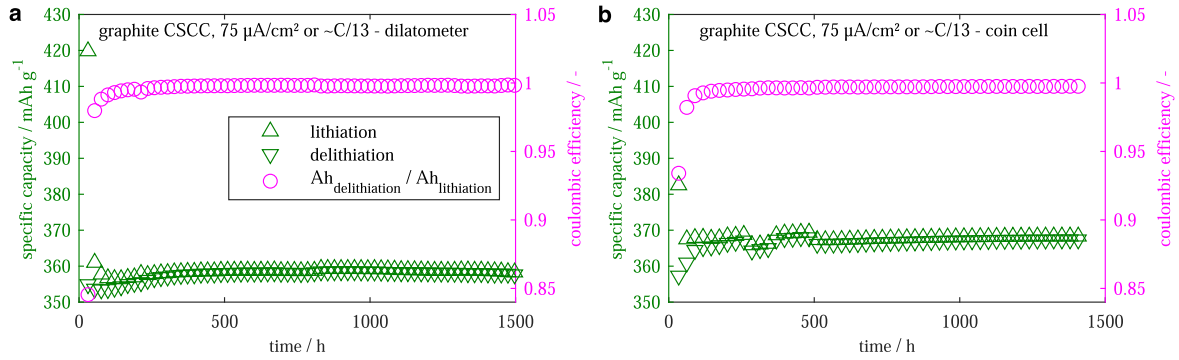

Figure 4. Specific charge/discharge capacities of a graphite electrode in the dilatometry cell (left) and in a coin cell (right) over 50 cycles (ca. 1500 h). Both cell types show good cycling stability and a coulombic efficiency of 99.7% – 99.8%. The two episodes of slightly elevated capacities of the coin cell coincide with and are likely caused by two episodes of ca. 5 K higher chamber temperature caused by a defective controller.

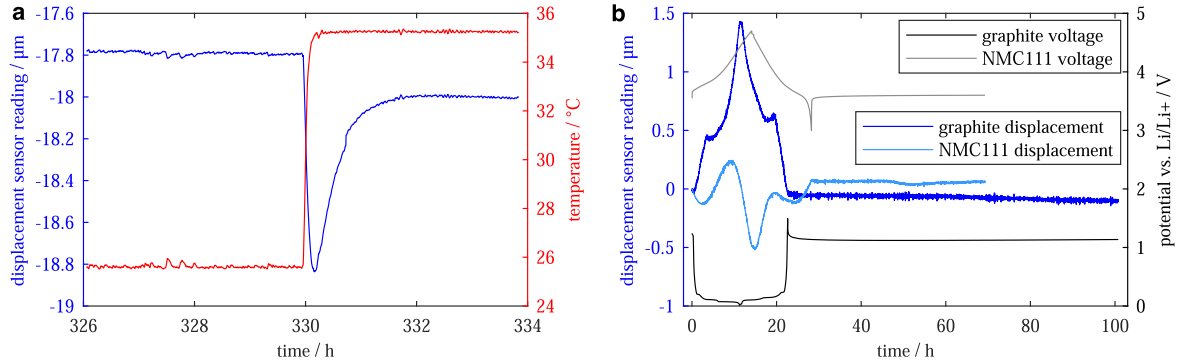

Figure 5. Displacement sensor reading vs time before and after a temperature shift (a) and during one full cycle followed by an OCV resting period of a graphite electrode and an NMC111 electrode spanning several days (b).

first three cycles, which may be due to its larger excess electrolyte volume, but after about 15 cycles, the coulombic efficiencies of both cells remained between 99.7% and 99.8%.

Reliability of the height change measurement.—The displacement sensor is mounted on a metal frame and there are intermediate metal parts between the sensor and the working electrode. Consequently, a measurement error related to thermal expansion of the instrument body can be expected. Additionally, capacitive sensors are inherently temperature sensitive due to changes to the dimensions of the sensor and guard electrode, the permittivity of the space between the electrodes and related alterations to edge effects and stray capacitances. Nojdelov et al.[23] describe these factors in detail and provide a typical compensation model for nm scales, which can be applied by the measurement electronics. Figure 5a shows the displacement sensor reading response for a cell containing a 60 μm thick graphite electrode to a chamber temperature shift from 25 °C to 35 °C. The reading dropped spontaneously by 1 μm and recovered 0.8 μm within 1.5 h, which is probably the time period necessary for full thermal equilibration of the dilatometer. Assuming 5.5e–5/K as thermal expansion coefficient for graphite, only 0.033 μm of the remaining deviation of 0.2 μm would be due to the expansion of the electrode itself. As the temperature fluctuations in the temperature chamber occur in shorter time frames, the more relevant measure should be the spontaneous drop of 1 μm or 0.1 μm K^{-1}, which is likely to be caused by a software correction factor. Another factor impacting the height change measurement is sensor drift. According to the manufacturer's specifications the drift is 20 nm h^{-1}. Figure 5b shows the relative displacement sensor reading during full cycles and subsequent resting periods of a 31 μm thick graphite electrode and a 64 μm thick NMC111 electrode. If the sensor drifted constantly at 20 nm h^{-1} in one direction during 80 h, the sensor reading would change by 1.6 μm. This is clearly not the case, as the reading change at the end of the 80 h resting period of the graphite electrode is less than 0.05 μm. The highest rate of change is measured at 50 h into the NMC111 experiment. Here a change of ca. 20 nm h^{-1} during 1 h is seen, which agrees with the specifications. In comparison to the 0.7 μm thickness change that this electrode undergoes during a cycle, the sensor drift appears to be negligible.

Results and Discussion

As the expansion of graphite electrodes has been studied in several publications, the decision was made to include an analysis of graphite to enable us to benchmark our results against previous measurements. The graphite dilatometry results will be discussed first, followed by a discussion of different nickel/manganese/cobalt/aluminum-based positive electrode materials and a harvested positive electrode from a commercial cell.

Graphite expansion: first cycles.—Two different graphite electrodes are discussed in this section, a flake-type graphite from SGL calendered to 35% porosity, and a non-calendered, spherical MCMB-type graphite from CSCC with a porosity of ca. 65%. Figures 6a/6b shows the height change and charge balance of the first 10 cycles of the SGL and CSCC[a] graphite electrodes. We will begin by focusing on the SGL graphite electrode. The height change upon first lithiation was 12.5%, accompanied by a 12% charge loss in the 1st cycle. The irreversible height change seen in the 1st cycle amounts to 7%. The initial expansion of this calendered graphite electrode was significantly larger than that reported so far for non-calendered graphite electrodes[19] as well as calendered electrodes.[22]

[a]Owing to a problem with a power connector in the long-term cycling experiment on CSCC graphite shown in Figs. 4b and 7b, the displacement sensor reading of the first 8 of the total of 50 cycles was lost. The experiment was repeated with a fresh electrode until 10 cycles were completed. This data is shown in Fig. 6.

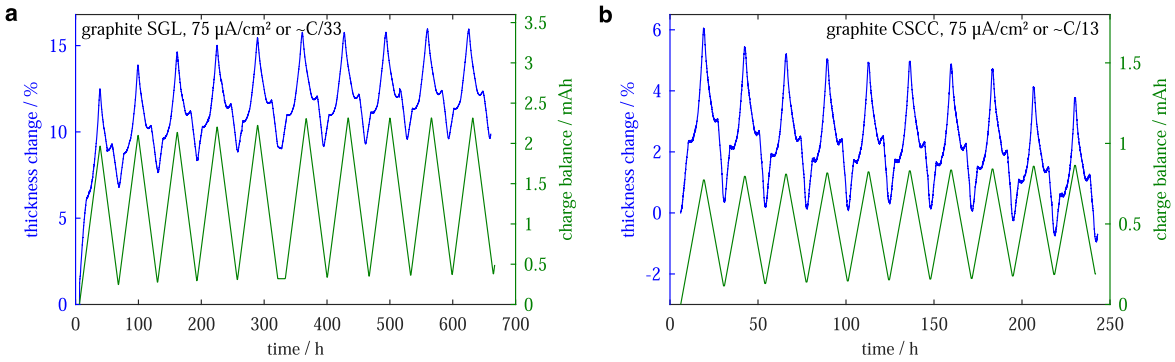

Figure 6. Thickness change and charge balance of SGL (calendered) and CSCC (non-calendered) graphite electrodes during the first 10 cycles. The initial irreversible thickness change in the calendered SGL electrode is significantly larger. The non-calendered CSCC electrode seems to contract rather than expand in the course of the first 10 cycles.

While the coulombic efficiency nears a plateau as early as the 2nd cycle, considerable irreversible height changes can be observed until the 5th cycle. Almost zero irreversible height change can be observed from the 8th to the 10th cycle, by which point the completely delithiated electrode has expanded by a total of 9% vs the fresh state. In contrast, the non-calendered CSCC electrode expanded by only 6% in the first cycle, and most of that expansion was reversed. Beginning with the 2nd cycle, and with the exception of cycle no. 5, the electrode contracted slightly more during each delithiation than it expanded on the preceding lithiation, leading to a net contraction of the electrode of −1% after 10 cycles or ca. −0.3 μm in 240 h. On the basis of the specified sensor drift, this result would fall within the margin of error. However, in light of the lower practical sensor drift shown in Fig. 5, it should not be prematurely rejected. In any case, the stark difference between the irreversible expansion of the calendered SGL electrode and the tendency to contract of the non-calendered CSCC electrode warrants explanation. It is conceivable that the calendered electrode reverses some of the compaction introduced by the calendering step: The first expansions and contractions of the particles may alter the morphology irreversibly in such a way that the expansions of the particle can be accommodated, leading to an overall expansion. This may be viewed as resulting from the structure's preference of minimizing elastic stress energy. In the non-calendered electrode, the expansions and contractions of the particles likely trigger a re-arrangement of the microstructure, too, but here the new local minimum of elastic stress energy may entail a more compact arrangement, leading to the slight overall contraction we observed. For a discussion of internal stress-strain relationships of electrodes the reader is referred to Rieger et al.[24]

Reversible expansion of graphite.—Figures 7a/7b shows potential and height change as a function of specific capacity. Six consecutive cycles of the SGL graphite and 20 consecutive cycles of the CSCC graphite illustrate the good reproducibility of both the voltage and the height change reading. Regarding the minor differences in the height change measurements with cycling, there is a weak trend towards decreasing change as the cycle number increases. In the dilatometry cell, the SGL graphite reaches a reversible capacity of 345 mAh g^{-1}—348 mAh g^{-1} with a height change of 6.5%, while the CSCC graphite reaches 357 mAh g^{-1} with 4.9% height change. The 6.5% height change of the calendered SGL graphite (35% porosity) agrees well with a previous measurement of a calendered graphite electrode in Rieger et al.[20] (33% porosity). The smaller height change of the non-calendered CSCC graphite seems to agree with results of non-calendered graphite electrodes in Hahn et al.,[19] although only first cycle data is presented in the study.

The numbers in Fig. 7b designate the different graphite stages. Their assignment to the voltage readings is based on Dahn et al.[25] and Asenbauer et al.[26] According to the "staging" mechanism of intercalants into graphite, the graphene layers are not occupied evenly by ions during lithiation, but in such a fashion, that one intercalant layer is completely filled before the next layer starts incorporating lithium ions. The intercalant layers are separated by a decreasing number of graphene layers as the lithiation progresses: In "stage 4," 4 graphene layers separate each intercalant layer, in "stage 1," only alternating layers of graphene and intercalant remain. For a comprehensive review of the "staging" mechanism the reader is referred to Bresser et al.[26] Figure 7a shows that, during lithiation, the electrode thickness increased linearly at first, reaching 1.8% when stage 3 is reached. During the transition between stage 3 and stage 2, which includes the "liquid" intermediate stage "2 l," the thickness increased at a much lower rate, reaching 2.3% at stage 2. Most of the height change, an additional 4.3%, occurred in the transition between stage 2 and stage 1. This progression is in qualitative

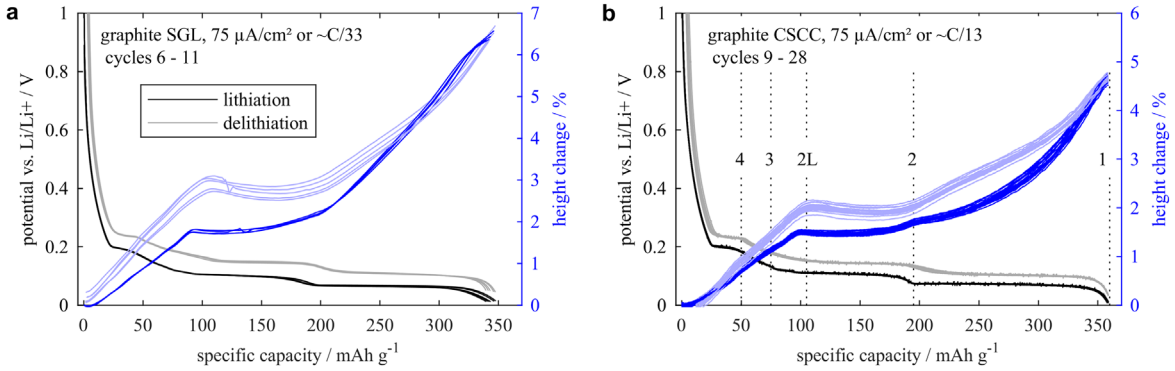

Figure 7. Thickness change vs specific capacity of SGL and CSCC graphite electrodes during multiple consecutive cycles. The thickness change on full lithiation is higher in the flake-type and calendered SGL graphite electrode than in the non-calendered MCMB-type CSCC graphite electrode.

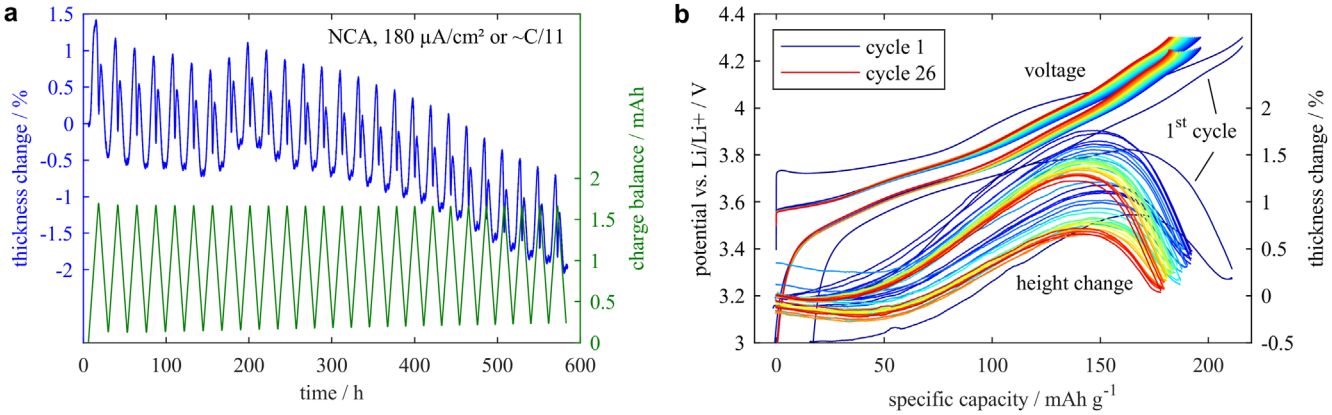

Figure 8. (a) Thickness change and charge balance, (b) voltage and thickness change per cycle during the first 26 cycles of an NCA electrode. The electrode contracted significantly during the first cycle, thereafter it generally seems to continue to contract slightly, but these reading changes are well within the specified sensor drift. Regarding the thickness changes within each cycle, there is a clear trend towards lower maximum expansions with higher cycle numbers.

agreement with measurements of interlayer spacing and unit cell volume evolution obtained via XRD.[25,27] In absolute terms, the interlayer spacing and the unit cell volume increase by ca. 10% and 13%[27] respectively, which would translate into a 4.2% ($\sqrt[3]{1.13} \approx 0.042$) thickness increase if random crystal orientation and hence isodirectional expansion are assumed. This is less, however, than the 6.5% thickness increase that was measured for the flake-type SGL graphite. Indeed, XRD-based studies have shown that the crystals in flake-type graphite electrodes are oriented preferentially in such a way that the intercalant layers are parallel to the current collectors.[28,29] In consequence, a thickness increase closer to the 10% interlayer spacing change would be expected, lessened only by the degree to which the particle volume change can be absorbed by the electrode structure, decreasing the porosity. For the flake-type graphite which expanded by 6.5%, this would mean that up to 3.5% of the solid particle volume may be absorbed by porosity reduction. Regarding the CSCC electrode made of spherical MCMB, which displayed reversible expansion of 4.9%, a more isodirectional expansion of the particles would be expected, making 4.2% the reference mark. As an explanation of this difference, it is conceivable that in such thin objects, strain is more likely to be released in the vertical direction than laterally.[24] However, this electrode was non-calendered and had a high porosity of 65%, providing plenty of room for accommodation of expanding particles. Unfortunately, the effect of initial electrode porosity on expansion cannot be clarified in this study because of the unfortunate sample combination of a calendered flake-type graphite electrode with a non-calendered spherical MCMB electrode.

NCA extended cycling.—In order to facilitate the interpretation of the following experiments in which various TMOs are compared, an NCA electrode was subjected to extended cycling over 580 h/26 cycles between 3.0 V and 4.3 V. The results are also shown here to give a sense of the displacement sensor drift when measuring TMOs, which expand significantly less than graphite. Figure 8a shows the thickness change and charge balance, Fig. 8b the voltage and thickness change per cycle. Figure 8a suggests that the NCA electrode contracted significantly during the first cycle, and then continued to contract at a lower variable rate, interrupted by a slight increase during cycles no. 8 and no. 9. All of these displacement sensor reading changes could be explained by the specified sensor drift: For example, the −0.15% change of the NCA electrode thickness from cycle no. 12 to no. 15 corresponds to only 83 nm in 66 h. However, observations of the sample after cycling, see Fig. 5b, demonstrate that the quantity of short-term drift significantly outweighs that of long-term drift. It also appears that the majority of the errors self-correct over a longer period. The thickness change measured by the dilatometer at the end of the experiment was −2% or 0.8 μm, however a post-experiment thickness measurement of the electrode using a micrometer screw yielded no change relative to before the experiment. The 1 μm resolution of the micrometer screw only allows the conclusion that the displacement sensor signal is probably accurate to within +−1 μm even after 580 h of continuous use. It is however unable to confirm the slight contraction of the NCA electrode measured by the displacement sensor.

A decrease in the magnitude of the thickness changes as the cycles progress is demonstrated by Fig. 8b. The slowing rate of this decrease suggests that a “steady state” would be reached upon continued cycling. The maximum expansion per cycle decreases from 1.7% in the first cycle, to 1.5% in the 6th cycle, to 1.2% in the 26th cycle, while the overall shape remains constant.

Comparison of different lithium-transition-metal-oxides.—The TMO electrodes were cycled to four different upper voltage cut-offs, 4.1 V, 4.3 V, 4.5 V and 4.7 V, for 3 cycles within each voltage window[b]. The cycling voltage profile is shown in Fig. 9a along with the coulombic efficiency of each cycle. At the end of the 30 min resting periods after each CC charging phase, the open-circuit voltages (OCV) were ca. 50 mV below the cut-off voltage. In two cases, Kokam 1st cycle and NMC622 4th cycle, the coulombic efficiency was higher than one. This was likely caused by temporary issues with the electrochemical cell, as in both cases there were alterations in the voltage signal during lithiation, perhaps due to incomplete wetting of smaller pores or gas bubbles at the electrode/T-frit/spacer interfaces. Otherwise, the highest coulombic efficiency was reached at the 3rd 3 V–4.3 V cycle. The lower efficiency at the 3rd 3 V–4.1 V cycle was probably due to initial side reactions taking place at a higher rate at that early stage. In each of the four sets of three cycles, coulombic efficiency dropped initially (compared to the 3rd cycle of the previous set of three) and then increased again. This indicates that every time a higher voltage regime was reached, new initial side reactions are triggered which then, at least partially, faded. At the 4.7 V cut-off, however, these side reactions seem to be more severe and persistent, as the reversible capacity was significantly diminished and all of the electrodes remained below 99% efficiency in the 3rd cycle. NMC111 and the Kokam cathode, which both have a relatively high cobalt content, have lower coulombic efficiencies at 4.7 V than the other materials. In light of the above, the different TMOs will be compared a) based on the 3rd cycle/4.3 V cut-off to study their thickness change in a highly stable regime and because the OCVs after the 30 min rest of about 4.25 V come close to the maximum voltages experienced by these electrodes in practical

[b]There are two exceptions: For NMC811, the first three cycles with 4.1 V cut-off were skipped due to a very large initial polarization. For the Kokam electrode, the first three cycles already had a 4.3 V cut-off, but were performed with a lower current.

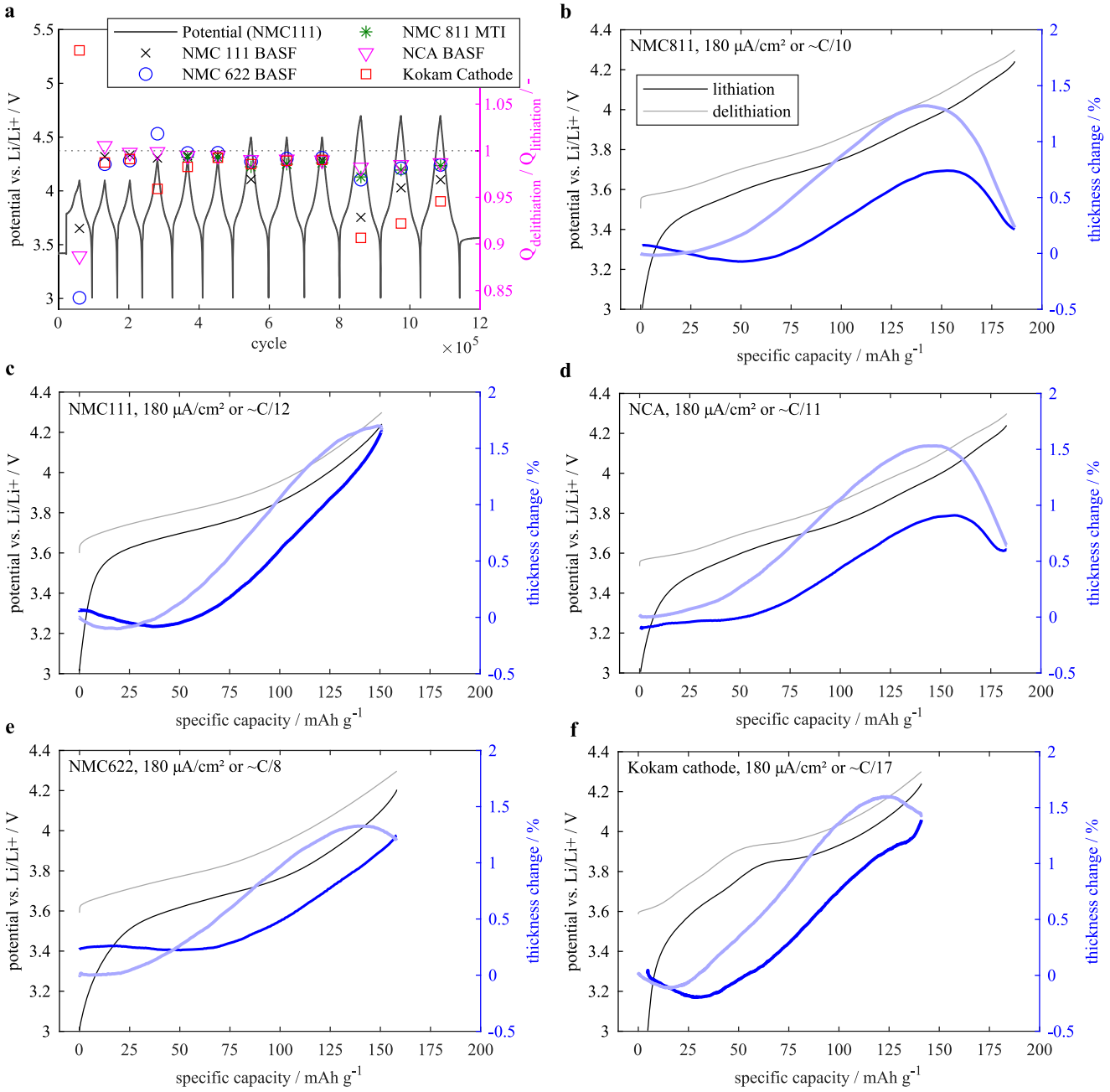

Figure 9. (a) Coulombic efficiency of TMO electrodes in the dilatometry cell for different upper-cut off voltages. (b)–(f) thickness change vs specific capacity of TMO electrodes during the 3rd cycle with a 4.3 V upper cut-off.

cells, b) based on the 1st cycle/4.7 V to discuss their thickness change at higher voltages. Regarding the latter, it should be pointed out that, for each individual material, the thickness change characteristics of cycles with different cut-off voltages agree well in their common voltage ranges. The NCA cycling results from the previous section suggest that the "steady state" thickness change characteristics upon continued cycling would be slightly reduced compared to those in the 6th and 9th cycles, which are analyzed in the following.

Figures 9b–9f show potential and height change vs specific capacity during the 3rd 3 V–4.3 V cycle for each of the TMO electrodes investigated here. Taking into account that the OCV after charging was ca. 50 mV below the cut-off voltage of 4.3 V, the reversible specific capacities of 150 mAh g^{-1} (NMC111), 158 mAh g^{-1} (NMC622), 187 mAh g^{-1} (NMC811) and 183 mAh g^{-1} (NCA) are in agreement with those in the literature.[30–33] Assuming an active material content of 96 wt-%, the Kokam cathode reaches 142 mAh g^{-1}. As its composition is proprietary, probably an NCA/LCO blend (see Fig. A·1, Appendix), there is no benchmark for the specific capacity.

The highest maximum expansion among the TMO electrodes tested here, was 1.7% and was measured for both the NMC111 and the Kokam cathodes. This was followed by NCA with 1.5% and NMC622 and NMC811 with 1.3%. The thickness changes of all the materials followed an S-shaped curve, with no expansion or a slight contraction at the beginning of delithiation, followed by a steep, almost linear increase, a subsequent leveling off of the expansion and a final contraction. There is significant hysteresis in the expansion/state-of-charge relationship: Differences in the thickness changes measured for a material during lithiation and delithiation reached a maximum of 0.5% of the initial sample thickness, or 30%–50% of the sample's maximum thickness change.

In the case of NMC111, NMC622 and the Kokam cathode, the expansion maximum coincides approximately with the end of charge

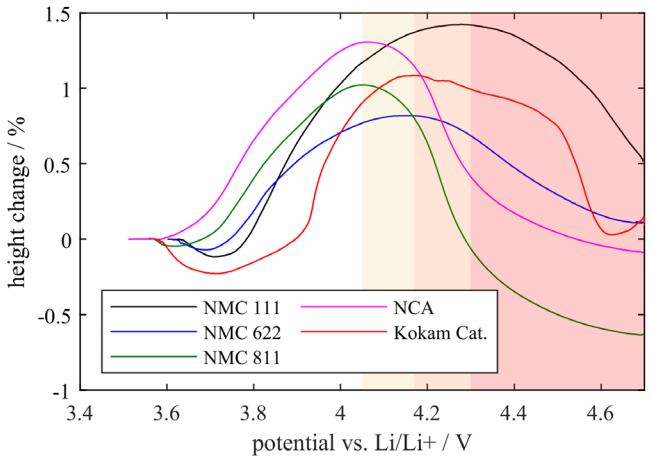

Figure 10. Thickness change of TMO electrodes vs voltage during delithiation. The higher the nickel content, the lower the voltage at which the electrodes reach their maximum expansion and start to contract.

to 4.3 V, but NMC811 and NCA contract abruptly during the last 20 mAh g^{-1} of delithiation, recuperating most of the previous expansion. Plotting the thickness change during the first delithiation to 4.7 V vs voltage as in Fig. 10, reveals that a higher nickel content correlates with a shift of the expansion maximum or beginning of contraction to lower voltages: NMC811 and NCA reached their maximum expansion at ca. 4.05 V (beginning of yellow shading), NMC622 and the Kokam cathode at ca. 4.15 V (orange shading) and NMC111 at 4.3 V (red shading). While NMC811 and NCA contracted strongly between 4.15 V and 4.3 V, NMC111 only contracted significantly above 4.4 V.

These differences in contraction at high voltages may be explained by results from XRD studies: In $Li(Ni_{1-x-y}Co_xMn_y)O_2$ materials, a phase transition involving a greatly reduced *c*-axis of the hexagonal lattice is suppressed or occurs at higher voltages when the content of nickel, relative to cobalt and manganese, is lower.[34,35] It has been reported that aluminum, may also help to suppress this phase transition.[36,37] This effect could explain why the contraction of the NCA electrode is less steep than that of NMC811 in the orange-shaded voltage region in Fig. 10.

Electrode expansion vs crystal structure change.—The $Li(Ni_{1-x-y}Co_xMn_y)O_2$ cathode is a layered crystalline structure of the α-$NaFeO_2$-type (space group $R\bar{3}m$, Z = 3). The absolute lengths as well as the change upon lithium insertion/extraction of the lattice parameters *a* and *c* of the hexagonal transition metal layers can be determined via operando XRD. The technique yields highly reproducible results, with differences of less than 1% between measurements of the NMC111 lattice parameters reported in different studies.[38–41] The following analysis uses XRD results from de Biasi et al.,[41] who investigated $Li(Ni_{1-x-y}Co_xMn_y)O_2$ electrodes with different nickel contents.

Figure 11 shows the change of the lattice parameters and the unit cell volume along with the thickness change registered by dilatometry of different NMC electrodes as a function of voltage. Both *a* and *c* change upon lithium extraction. The magnitude of this change is more drastic for high nickel NMCs. Initially, *a* decreases in a linear fashion until 4.0 V, then remains constant until 4.4 V where it begins to increase again. The drastic initial decrease can be attributed to the decreasing ionic radii of the transition metals as they are oxidized in the delithiation process. With *c*, the opposite trend can be seen. It initially expands until a potential of 4.0 V is reached, followed by a plateau until 4.2 V. At higher voltages, *c* decreases drastically. The initial expansion in *c* is attributed to increasing coulomb repulsion upon lithium extraction from interslab sites. As the extraction of lithium proceeds, the interslab width contracts due to the emergence of empty sites and *c* decreases. While the evolution of *a* is quite similar in all three NMCs, the slope of *c* varies strongly with the relative nickel content: In NMC811 (Fig. 11c), the contraction of *c* is much more pronounced than in NMC622 (b) and NMC111 (a) and is shifted towards lower voltages. The unit cell volume of NMC in hexagonal closed pack (hcp) configuration, $V = \frac{\sqrt{3}a^2c}{2}$, has a quadratic dependence on *a* and a linear dependence on *c*. Consequently, as long as *a* and *c* evolve in opposite directions, the unit cell volume roughly follows *a* until, above 4.2 V, it follows the strong decrease of *c*.

The electrode thickness as measured by dilatometry agrees best with *c*, or, also displayed in Fig. 11, the sum of *a* and *c*. Given that the investigated materials are all polycrystalline and contain a collection of randomly orientated layered-oxide grains, this seems counter intuitive as one could expect the unit cell volume to determine the thickness evolution. This was found to be the case for a $LiCoO_2$ electrode, where a unit cell volume change of +2.32% triggered a thickness increase of ca. 1.8%.[24] However, it may be that microscopic expansions in all directions lead to elastic, reversible macroscopic expansions while contractions, rather than leading to macroscopic contractions, instead lead to an increase of void space in the electrode structure. This could be explained by the binder forming a type of skeleton which provides stability against compression but out of which the microstructure could expand. The existence of such a structure would explain why the thickness change follows the growth of *c* and shrinking back to its initial value but seems largely unaffected by both the shrinking of *a* and the further shrinking of *c* to negative relative values. At this juncture, the inflexible binder skeleton would prevent a further reduction in thickness being measured. A minor divergence from that overall

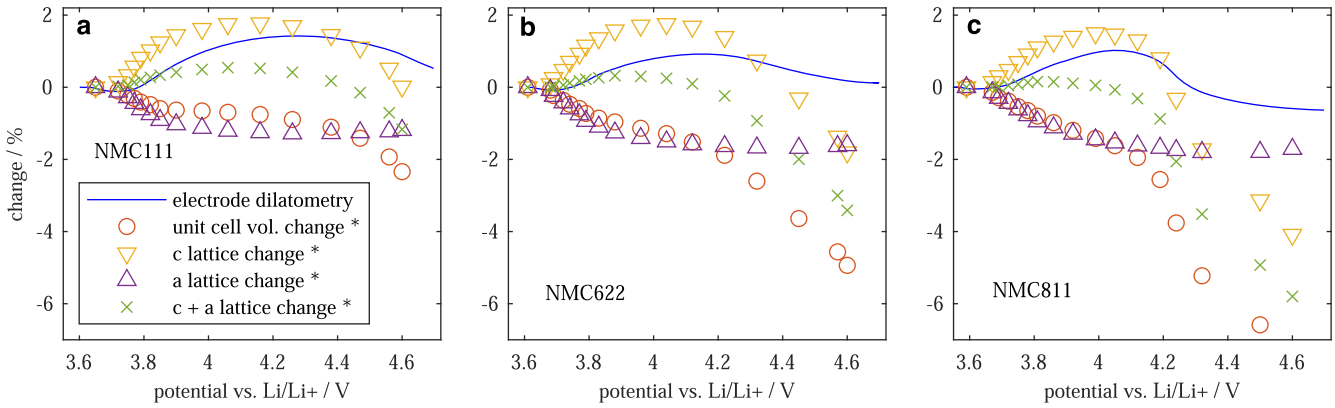

Figure 11. Thickness change of TMO electrodes compared to crystal structure changes measured via XRD. Electrode thickness change correlates weakly with the c lattice parameter, but does not follow the unit cell volume, especially at higher voltages, where the unit cell volume decreases significantly. All XRD data (marked with *) are reproduced from de Biasi et al.[41]

behavior occurs at the beginning of the lithium extraction, where all electrodes contract slightly and the sum of *a* and *c* agrees better with the electrode thickness evolution than c alone. Regarding the magnitude of the changes, it is plausible, as with the graphite electrodes discussed above, that the percentage electrode thickness change is smaller than the largest unidirectional lattice expansion occurring at the microscopic level. This may be due to some absorption of the particle expansion by the electrode structure, reducing the porosity, and the non-preferential orientation of the grains.

Conclusions

A dilatometry setup was validated and used to investigate the thickness changes of various negative and positive electrode materials used in lithium-ion batteries. By operating the dilatometry setup in a temperature-controlled argon atmosphere, cycling stability comparable to coin cells and high reproducibility of the dilation measurements was achieved. It was shown that the uncertainty related to drift of the capacitive displacement sensor is negligible compared to the dilation even of transition metal oxide electrodes with relatively low areal loadings. For two different types of graphite electrodes, maximum reversible thickness changes of 4.9% (spherical MCMB type) and 6.5% (flake type) were obtained. It could not be established to which extent this difference was caused by calendering, resulting in different electrode porosities, or by the particle type. In the case of the flake type graphite, we argued that due to preferential orientation of crystals, the interlayer spacing change of ca. 10% is a more adequate reference measure than the ca. 4.2% isodirectional expansion that would result from the unit cell volume change under the assumption of random crystal orientation. This raised the question of how much of the particle volume change is absorbed by the porous structure of the electrode, and an upper limit of ca. 3.5% was calculated. TMO electrodes showed maximum expansions of 1.3% to 1.7% upon delithiation to an equilibrium potential of ∼4.25 V, and, when further delithiated to an equilibrium potential of ∼4.65 V vs Li/Li+, contractions of up to −0.5% vs the fully lithiated state. Higher nickel contents seemed to reduce the equilibrium potential at which the expansion reached its maximum and contraction began. Finally, electrode thickness changes were compared to crystal structure change data from scientific literature. No correlation could be established between the expansion of the porous composite electrodes and the unit cell volume change, although a relationship to the evolution of the *c* lattice parameter of the hexagonal layered structure suggested itself. The results also indicated that a contraction that takes places in the crystal structure or on the primary particle level does not necessarily lead to a contraction on the electrode level. This study demonstrated that electrode level thickness changes as a result of lithiation and delithiation can be measured with high accuracy in a dilatometry cell and that extrapolating such changes from the structural change of active materials at the single-crystal level involves significant uncertainty.

Acknowledgments

We thank former student research assistant Igor Senna for his help with electrode preparation and preliminary dilatometry experiments. We thank Stefan Oswald (TUM, Germany) for his advice regarding electrode preparation and for fruitful discussions and Fabian Linsenmann (TUM) for more fruitful discussions. We also thank Prof. Chia-Chin Chang of the National University of Tainan, Taiwan, and Dr. Shang-Chieh Hou of the National Cheng Kung University, Taiwan, for providing the CSCC graphite electrodes. This work was financially supported by the German Federal Ministry of Education and Research (BMBF) in the projects HighSafe (03XP0138B), HighSafe II (03XP0306B), ExZellTUM II (03XP0081), ExZellTUM III (03XP0255) and by the Technical University of Munich. The responsibility for this publication rests with the authors.

Appendix

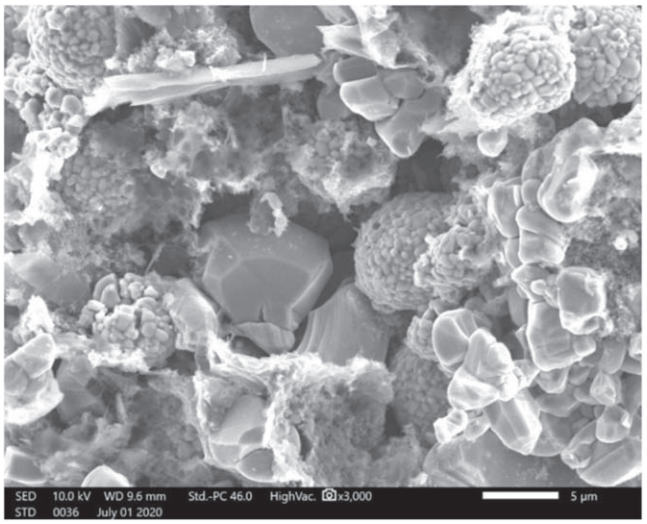

Figure A·1. SEM image of the Kokam cathode. A cobalt/nickel ratio of 8/5 was detected by EDX, with no manganese present. Comparison to SEM images of NCA and LCO electrodes[42–44] suggests it is an NCA/LCO blend, which has been reported for other types of Kokam pouch cells.

Table A·I. Slurry recipes of the electrodes prepared for this study.

Type	Component	Fraction of solid content/wt.-%
Graphite (SGL)	Active material	95.0
	PVDF Kynar HSV900	5.0
	NMP	45.0 (of total mass)
Graphite (CSCC)	Active material	95.0
	MMM Carbon SuperP	2.0
	Sigma-Aldrich CMC/Zeon Co. SBR	2.5/0.5
	De-ionized water	65.0 (of total mass)
NMC 111 (BASF)	Active material	96.0
	PVDF Solvay Solef 5130	2.0
	Timcal Super C65	2.0
	NMP	37.50 (of total mass)
NMC 622 (BASF)	Active material	92.50
NMC 811 (MTI)	PVDF Solvay Solef 5130	3.50
NCA (BASF)	Timcal Super C65	4.0
	NMP	46.50 (of total mass)

ORCID

Franz B. Spingler https://orcid.org/0000-0002-6523-3986
Simon Kücher https://orcid.org/0000-0003-2230-7356
Robert Phillips https://orcid.org/0000-0001-7332-6739
Erfan Moyassari https://orcid.org/0000-0002-3037-202X
Andreas Jossen https://orcid.org/0000-0003-0964-1405

References

1. J. Gonzalez, K. Sun, M. Huang, J. Lambros, S. Dillon, and I. Chasiotis, *J. Power Sources*, **269**, 334 (2014).
2. L. Y. Beaulieu, T. D. Hatchard, A. Bonakdarpour, and M. D. Fleischauer, *J. Electrochem. Soc.*, A1457 (2003).
3. R. Xu and K. Zhao, *J. Electrochem. En. Conv. Stor.*, **13**, 30803 (2016).
4. A. O. Kondrakov, A. Schmidt, J. Xu, H. Geßwein, R. Mönig, P. Hartmann, H. Sommer, T. Brezesinski, and J. Janek, *J. Phys. Chem. C*, **121**, 3286 (2017).
5. Y. H. Choi, H. K. Lim, J. H. Seo, W. J. Shin, J. H. Choi, and J. H. Park, *SAE International Journal of Alternative Powertrains*, **7**, 195 (2018).
6. S. Mohan, Y. Kim, J. B. Siegel, N. A. Samad, and A. G. Stefanopoulou, *J. Electrochem. Soc.*, **161**, A2222 (2014).
7. N. A. Samad, Y. Kim, J. B. Siegel, and A. G. Stefanopoulou, *J. Electrochem. Soc.*, **163**, A1584 (2016).
8. C. M. DeLuca, K. Maute, and M. L. Dunn, *J. Power Sources*, **196**, 9672 (2011).
9. M. L. Terranova, S. Orlanducci, E. Tamburri, V. Guglielmotti, and M. Rossi, *J. Power Sources*, **246**, 167 (2014).
10. P. K. Leung, C. Moreno, I. Masters, S. Hazra, B. Conde, M. R. Mohamed, R. J. Dashwood, and R. Bhagat, *J. Power Sources*, **271**, 82 (2014).
11. B. Rieger, S. F. Schuster, S. V. Erhard, P. J. Osswald, A. Rheinfeld, C. Willmann, and A. Jossen, *Journal of Energy Storage*, **8**, 1 (2016).
12. C. Birkenmaier, B. Bitzer, M. Harzheim, A. Hintennach, and T. Schleid, *J. Electrochem. Soc.*, **162**, A2646 (2015).
13. I. Soga and Y. Kinoshita, *Japan. J. Appl. Phys.*, **41**, 6616 (2002).
14. B. Bitzer and A. Gruhle, *J. Power Sources*, **262**, 297 (2014).
15. Z. J. Schiffer, J. Cannarella, and C. B. Arnold, *J. Electrochem. Soc.*, **163**, A427 (2015).
16. J. H. Lee, H. M. Lee, and S. Ahn, *J. Power Sources*, **119-121**, 833 (2003).
17. M. Nagayama, K. Ariyoshi, Y. Yamamoto, and T. Ohzuku, *J. Electrochem. Soc.*, **161**, A1388 (2014).
18. D. Sauerteig, S. Ivanov, H. Reinshagen, and A. Bund, *J. Power Sources*, **342**, 939 (2017).
19. M. Hahn, H. Buqa, P. W. Ruch, D. Goers, M. E. Spahr, J. Ufheil, P. Novák, and R. Kötz, *Electrochem. Solid-State Lett.*, **11**, A151 (2008).
20. B. Rieger, S. Schlueter, S. V. Erhard, J. Schmalz, G. Reinhart, and A. Jossen, *J. Energy Storage*, **6**, 213 (2016).
21. W. Biberacher, A. Lerf, J. O. Besenhard, H. Möhwald, and T. Butz, *Mater. Res. Bull.*, **17**, 1385 (1982).
22. H. Michael, F. Iacoviello, T. M. M. Heenan, A. Llewellyn, J. S. Weaving, R. Jervis, D. J. L. Brett, and P. R. Shearing, *J. Electrochem. Soc.*, **168**, 10507 (2021).
23. M. R. Nojdelov, D. Dirk Voigt, M. Arthur, S. van de Nes, and M. S. Nihtianov, *2015 9th International Conference on Sensing Technology (ICST): 2015 9th International Conference on Sensing Technology (ICST) took place 8-11 December 2015 in Auckland* (IEEE, New Zealand, Piscataway, NJ) (2015).
24. B. Rieger, S. Schlueter, S. V. Erhard, and A. Jossen, *J. Electrochem. Soc.*, **163**, A1595 (2016).
25. J. Dahn, *Phys. Rev. B*, **44**, 9170 (1991).
26. J. Asenbauer, T. Eisenmann, M. Kuenzel, A. Kazzazi, Z. Chen, and D. Bresser, *Sustainable Energy Fuels*, **4**, 5387 (2020).
27. S. Schweidler, L. de Biasi, A. Schiele, P. Hartmann, T. Brezesinski, and J. Janek, *J. Phys. Chem. C*, **122**, 8829 (2018).
28. P. Baade, M. Ebner, and V. Wood, *J. Electrochem. Soc.*, **164**, E348 (2017).
29. S. Malifarge, B. Delobel, and C. Delacourt, *J. Power Sources*, **343**, 338 (2017).
30. T. Ohzuku and Y. Makimura, *Chem. Lett.*, 642 (2001).
31. P. Y. Liao, J. G. Duh, and S. R. Sheen, *J. Power Sources*, **143**, 212 (2005).
32. R. Robert and P. Novak, *J. Electrochem. Soc.*, **162**, A1823 (2015).
33. M.-H. Kim, H.-S. Shin, D. Shin, and Y.-K. Sun, *J. Power Sources*, **159**, 1328 (2006).
34. W.-S. Yoon, K. Y. Chung, J. McBreen, and X.-Q. Yang, *Electrochem. Commun.*, **8**, 1257 (2006).
35. J. Xu, E. Hu, D. Nordlund, A. Mehta, S. N. Ehrlich, X.-Q. Yang, and W. Tong, *ACS Appl. Mater. Interfaces*, **8**, 31677 (2016).
36. T. Ohzuku, T. Yanagawa, M. Kouguchi, and A. Ueda, *J. Power Sources*, **68**, 131 (1997).
37. M. Guilmard, *J. Power Sources*, **115**, 305 (2003).
38. J.-M. Kim and H.-T. Chung, *Electrochim. Acta*, **49**, 937 (2004).
39. S.-C. Yin, Y.-H. Rho, I. Swainson, and L. F. Nazar, *Chem. Mater.*, **18**, 1901 (2006).
40. X.-L. Wang et al., *Sci. Rep.*, **2**, 1 (2012).
41. L. de Biasi, A. O. Kondrakov, H. Geßwein, T. Brezesinski, P. Hartmann, and J. Janek, *J. Phys. Chem. C*, **121**, 26163 (2017).
42. E. J. Cheng, N. J. Taylor, J. Wolfenstine, and J. Sakamoto, *Journal of Asian Ceramic Societies*, **5**, 113 (2017).
43. M. Ebner, D.-W. Chung, R. E. García, and V. Wood, *Adv. Energy Mater.*, **4** (2014).
44. P. Xiao, T. Lv, X. Chen, and C. Chang, *Sci. Rep.*, **7**, 1408 (2017).